Journal Pre-proof

Multimaterial DLP Printing with Centrifugal-Assisted Rinsing and Inverse Design of Voxel Structures

Mengjie Zhang , Dong Wang , Liguo Hu , Le Dong , Kun Zhou , Qi Ge , Guoying Gu

PII: S2667-3258(26)00033-6
DOI: https://doi.org/10.1016/j.fmre.2026.01.016
Reference: FMRE 1208

To appear in: *Fundamental Research*

Received date: 10 August 2025
Revised date: 9 January 2026
Accepted date: 26 January 2026

Please cite this article as: Mengjie Zhang , Dong Wang , Liguo Hu , Le Dong , Kun Zhou , Qi Ge , Guoying Gu , Multimaterial DLP Printing with Centrifugal-Assisted Rinsing and Inverse Design of Voxel Structures, *Fundamental Research* (2026), doi: https://doi.org/10.1016/j.fmre.2026.01.016

Multimaterial DLP Printing with Centrifugal-Assisted Rinsing and Inverse Design of Voxel Structures

Mengjie Zhang[1], Dong Wang[1,2], Liguo Hu[1], Le Dong[1], Kun Zhou[3], Qi Ge[4*], Guoying Gu[1,2*]*

1. State Key Laboratory of Mechanical System and Vibration, School of Mechanical Engineering, Shanghai Jiao Tong University, Shanghai 200240, China
2. Shanghai Key Laboratory of Intelligent Robotics, Shanghai Jiao Tong University, Shanghai 200240, China
3. Singapore Centre for 3D Printing, School of Mechanical and Aerospace Engineering, Nanyang Technological University, 50 Nanyang Avenue, Singapore 639798, Singapore
4. Department of Mechanical and Energy Engineering, Southern University of Science and Technology, Shenzhen, 518055, China

*To whom correspondence may be addressed. Email: wang_dong@sjtu.edu.cn (D.W.), geq@sustech.edu.cn (Q.G.), guguoying@sjtu.edu.cn (G.Y.G.)

Abstract

Voxel structures provide precise control over material distribution at the microscale. The integrated material–structure design paradigm offers a broader design space than traditional approaches based solely on geometry or homogeneous materials. A fundamental question in voxel structures is how to accurately print each voxel with designed sizes while avoiding interfacial contamination. To address it, we develop a multimaterial DLP 3D printer that integrates centrifugal forces and liquid rinsing, significantly reducing interfacial contamination, especially for high-viscosity resins. Additionally, we establish a multiphysics model considering chemical reactions, diffusion effects, and Gaussian light fields to predict voxel sizes accurately. This model is applicable to multiple resin types and is used to optimize printing parameters for individual voxels. By combining the fabrication method and theoretical model, voxel structures can be fabricated with high precision, facilitating the design of diverse functional behaviors. Hence, a machine learning-evolution algorithm method is developed to inversely design voxel distribution across a vast design space, and voxel structures with tailored buckling behaviors are demonstrated. The proposed fabrication, modeling, and design framework pave the way for developing voxel structures.

Keywords: voxel structures, multimaterial DLP 3D printing, multiphysics modeling, Python-assisted FE simulations, ML-EA optimization

1. Introduction

Voxels, the 3D counterparts of pixels, serve as the fundamental building blocks of 3D objects [1-3]. Voxel structures consist of discrete programmable voxels, each of which can be individually tailored at the microscale level in terms of size, shape, and material, allowing for precise control over macroscale behavior [4-8]. The integrated material–structure design paradigm offers a broader design space than traditional approaches based solely on geometry or homogeneous materials, which is promising in metamaterials [9], soft robotics [10,11], and biomedical fabrication [12]. A fundamental question in voxel structures is how to accurately print each voxel with designed sizes while avoiding interfacial contamination [13,14].

Many novel multimaterial 3D printing technologies have been reported for fabricating voxel structures [15], including inkjet-based 3D printing [8,16,17], multi-nozzle direct ink writing method [3,4], and multimaterial Digital Light Processing (DLP) 3D printing. Among them, DLP 3D printing offers precise material distribution, complex structural design, and strong interfacial bonding [18,19]. However, interfacial contamination is a major issue in DLP 3D voxel printing. To reduce it, several approaches have been proposed, such as injecting resins through microfluidic conduits into a continuous liquid interface [20], dynamic fluidic control for in-situ resin switching [21,22], removing residual resin by air jetting [19], and centrifugal force-assisted cleaning [23]. **Table 1** summarizes the viscosity range of currently reported methods for voxel printing. The highest reported resin viscosity is 2.7 Pa·s. However, the ability to print higher-viscosity resins is also essential, as they offer advantages in material properties and functionality. Existing methods, however, are not well-suited for such resins and tend to result in significant interfacial contamination. Therefore, a reliable approach for fabricating voxel structures using high-viscosity resins remains elusive.

Furthermore, trial-and-error experimentation is insufficient for accurately fabricating small voxels due to the complexity of the curing process [24,25], which involves chemical reactions [26], diffusion effects [27], and a non-uniform Gaussian light field [28,29]. This challenge is particularly critical in voxel structures, where fabrication inaccuracies can lead to structural

failure or material interference. For example, under-curing can lead to structural failures at voxel interfaces, while over-curing can cause material interference, where one material occupies the region designated for another. Several theoretical models have been developed to predict the shape of printing structures, such as polymerization reaction kinetics [26], reaction-diffusion model [27], multiphysics model considering light field effects [28,29], coupled photo-chemo-mechanical theoretical framework [30], and spatiotemporal model and optimization of grayscale DLP printing [31]. For voxel 3D printing, the theoretical model must be generalizable across different resin types. In addition, diffusion effects play a critical role and should be accounted for.

Herein, we developed a multimaterial DLP 3D printing platform (**Fig. 1(a)** and (b)) that integrates centrifugal force-assisted resin removal and liquid-based rinsing. The combination of centrifugation and liquid rinsing effectively eliminates cross-contamination between different materials, even for high-viscosity resins (Fig. 1(c)). A detailed comparison can be found in Supplementary Materials (Table S2). We developed a multiphysics model that accounts for chemical reactions, diffusion effects, and Gaussian light fields to accurately predict voxel sizes. Using this model, we have obtained the optimal printing parameters for each resin (Fig. 1(d)). By combining the fabrication technology and theoretical model, voxel structures can be accurately fabricated, which can facilitate the design of various behaviors [32-37]. We then developed a Machine Learning-Evolution Algorithm (ML-EA) method to inversely design the voxel distribution across a vast design space. (Fig. 1(e)) A buckling voxel structure is taken as an example to achieve optimal force–strain curves, maximizing energy absorption while minimizing force variations (Fig. 1(f)). The proposed fabrication and modeling framework paves the way for the design of voxel structures.

Table 1. The viscosity range of currently reported DLP methods for voxel printing.

	This work	Kowsari et al., 2018 [19]	Wang et al. 2022 [38]	Cheng et al.,2022 [23]	He et al., 2025 [39]	Yang et al., 2024 [40]

Viscosity /Pa·s	0.001~4.58	0.15	0.001~0.01	0.001~2.7	0.001~1.4	0.001

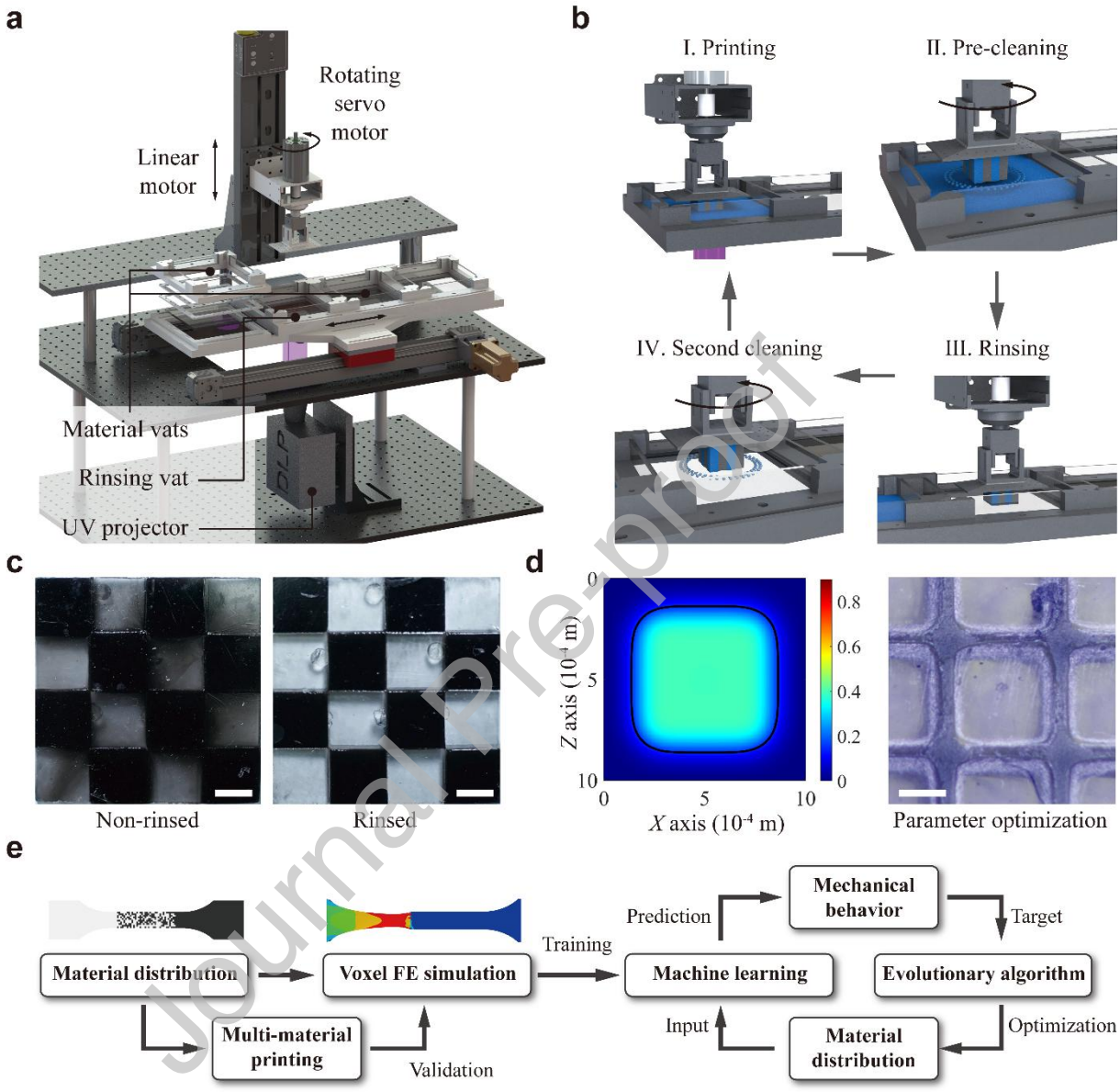

Fig. 1. Multimaterial DLP 3D printing. (a) Schematic illustration of the multimaterial DLP 3D printing system. (b) The printing procedure. Step I: image projection and curing; Step II: centrifugal pre-cleaning in the current vat; Step III: solvent rinsing; Step IV: second centrifugal cleaning to remove residual resin and solvent. (c) Comparison of non-rinsed and rinsed checkerboard samples. (Scale bar: 5 mm) (d) Theoretical model guiding the parameter optimization to eliminate material interference. (Scale bar: 0.5 mm) (e) The workflow of the voxel-based FE simulation and ML-EA method.

2 Results and discussion

2.1 Solvent-assisted multimaterial DLP 3D printing system

A custom multimaterial DLP 3D printing system was developed (Fig. 1(a)). It includes multiple vats mounted on a horizontal translation stage for automatic vat selection. One vat contains rinsing agents (ethanol), while the others hold various photopolymer resins for curing. A UV projector (theoretical optical resolution: 50 μm/pixel) projects UV light patterns onto the bottom of the resin vat to cure each layer. Each vat is equipped with a Perfluoroalkoxy (PFA) membrane to separate the printed structure from the vat. The printing platform, mounted on a vertical translation stage, is driven by a rotating servo motor, which ensures both high-speed rotation for cleaning and precise orientation.

The printing procedure is shown in Fig. 1(b). To print material A, the corresponding resin vat is positioned at the center, and the platform descends according to the desired thickness. The slice image for material A is projected to cure the layer (Step I). The platform is then lifted, separating it from the resin surface, and the rotating motor begins pre-cleaning of residual resin in the current vat (Step II). The in situ collection of the residual resin largely decreases the resin cost. Next, the platform is raised above the resin vat, the rinsing vat is centered, and the platform is submerged in the rinsing agent (Step III). Low-speed spinning in the rinsing agent ensures thorough rinsing, followed by high-speed spinning to remove any remaining rinsing agent and resin (Step IV). The final spin ensures that no rinsing agent interferes with the crosslinking of subsequent layers. The same procedure is applied when switching to material B.

2.2. The solvent effect on contamination removal

Previous work used high-speed centrifugal force (6000-10,000 rpm) to remove residual material [23], which is inefficient for high-viscosity resins (>1 Pa·s) and may damage the printed soft structures. The addition of the rinsing agent addressed these issues. Three rinsing agents were tested, and 95% ethanol was chosen as the rinsing agent in this work (**Fig. S1** and

Fig. S2). The cleaning effectiveness of the rinsing agent was evaluated for three resins with different viscosities: VeroBlack (0.15 Pa·s), F69 (1.40 Pa·s), and EAUD (4.58 Pa·s). Resin thicknesses after rotation ($t_2 - t_1$) with and without rinsing were measured (**Fig. 2(a)** and (b)). Note that the real printing platform in the DLP system is down-facing (Fig. 1(a)), while the setup in Fig. 2(a) is designed for resin thickness characterization. The platform is oriented upward in this test to enable controlled dispensing and measurement of residual resin, and gravity effects are negligible compared with centrifugal acceleration.

The total rotational time was set to 16 s in all tests. Residual thicknesses below 10 μm were considered acceptable with no significant cross-contamination. As shown in Fig. 2(b), the non-rinsed samples required higher speeds: 5000 rpm for VeroBlack and 8000 rpm for F69. In contrast, the rinsed samples achieved similar results at a much lower speed (3000 rpm for both resins), with nearly 100% contamination removal at 6000 rpm. For EAUD, the residual thickness was 26 μm even at 10,000 rpm without rinsing, making it unsuitable for multimaterial printing. However, rinsing reduced the residual thickness to nearly zero.

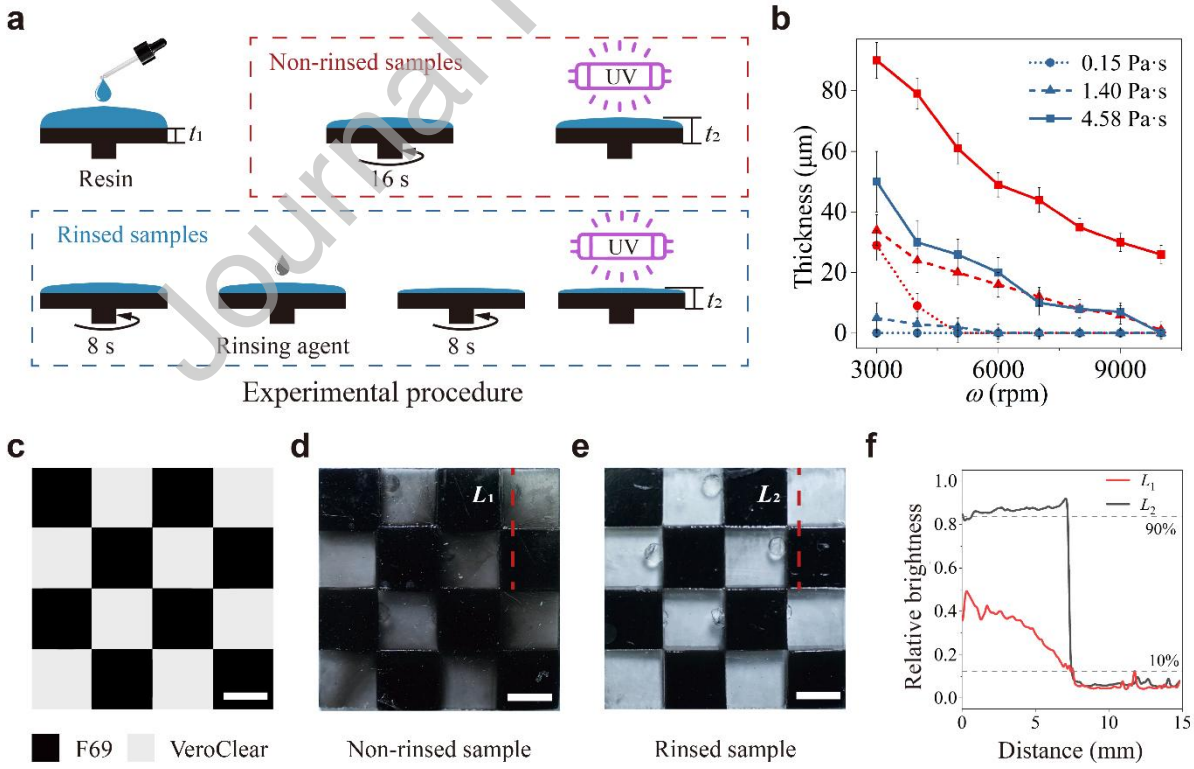

Fig. 2. Effectiveness of solvent rinsing in removing contamination. (a) Experimental procedure

for contamination comparison. (b) Residual resin thickness as a function of rotational speed for three resins with varying viscosities (Red lines: non-rinsed samples; Blue lines: rinsed samples). (c) A two-material checkerboard pattern designed for contamination comparison. (d),(e) Snapshots of the two-material printed samples without and with the rinsing step. (f) Relative brightness profile along lines L_1 and L_2. (Scale bar: 5 mm)

Two-material checkerboards with a thickness of 1.5 mm were 3D printed using F69 (black) and VeroClear (transparent) for comparison (Fig. 2(c)). The rotation speed was set to 6000 rpm. Samples without rinsing showed obvious contamination (Fig. 2(d)), with the transparent areas heavily contaminated by the black resin. In contrast, rinsed samples displayed no visible contamination in the transparent areas (Fig. 2(e)). Quantitative analysis of relative brightness (RB) values was performed to assess contamination levels. The RB values along lines L_1 and L_2 also show sharp boundaries between the two materials after rinsing (Fig. 2(f)). The RB curve of the rinsed sample showed an apparent drop at the material interface compared to the non-rinsed one, indicating a clear interfacial boundary.

2.3. Theoretical model for printing size estimation

Although solvent-assisted multimaterial DLP 3D printing effectively eliminates cross-contamination, the accurate assignment of voxels requires the development of theoretical models that can predict the voxel size. A theoretical model considering chemical reactions, diffusion effects, and Gaussian light fields was developed.

The polymerization process includes complex physicochemical reactions. When a photoinitiator (PI) absorbs photons, it decomposes into two active radicals R* at a decomposition rate of K_d. The symbol * represents the active site. These radicals react with monomers M at an initiation rate of K_i, forming active monomers RM*. These active monomers propagate polymer chains at a rate of K_p, and chain termination occurs at a rate of K_t [26,41,42]. Oxygen involvement is neglected due to the absence of an oxygen-permeable window. The reaction can be summarized as

$$\mathrm{PI} \xrightarrow{K_d} 2\mathrm{R}^*, \tag{1}$$

$$R^{*}+M \xrightarrow{K_i} RM^{*}, \tag{2}$$

$$RM_n^{*}+M \xrightarrow{K_p} RM_{n+1}^{*}, \tag{3}$$

$$RM_n^{*}+RM_m^{*} \xrightarrow{K_t} RM_{m+n}R/RM_n+RM_m. \tag{4}$$

Considering chemical species diffusion, a photopolymerization kinetics model is developed:

$$\frac{\partial C_I}{\partial t} = D_I \nabla^2 C_I - K_d C_I I, \tag{5}$$

$$\frac{\partial C_R}{\partial t} = D_R \nabla^2 C_R + 2K_d C_I I - K_i C_M C_R, \tag{6}$$

$$\frac{\partial C_{RM}}{\partial t} = D_{RM} \nabla^2 C_{RM} + K_i C_M C_R - K_t C_{RM}^2, \tag{7}$$

$$\frac{\partial C_M}{\partial t} = D_M \nabla^2 C_M - K_p C_M C_{RM} - K_i C_M C_R. \tag{8}$$

The variables C_I, C_R, C_{RM}, and C_M represent the concentration of the photoinitiators, radicals, active monomers, and monomers, respectively. The variable diffusion coefficient D_j ($j = I, R, RM, M$) is defined as [27]

$$\frac{1}{D_j(t)} = \frac{1-\phi}{D_j^{Liquid}} + \frac{\phi}{D_j^{Solid}}, \tag{9}$$

where D_j^{Liquid} and D_j^{Solid} represent the diffusion coefficients of specific species in the liquid phase and solid phase. The degree of conversion (DoC) ϕ is expressed as the reduction of monomers

$$\phi = 1 - \frac{C_M}{C_M(t=0)}. \tag{10}$$

The light field I is the superposition of all projected pixels

$$I(x,y,z) = \sum_{i=1}^{n} I_i(x,y,z), \tag{11}$$

where I_i is the light intensity distribution projected from each pixel. It follows the Gaussian distribution [24,28,31]

$$I_i(x, y, z = 0) = I_0 \exp\left[-2\frac{(x_i - x_0)^2 + (y_i - y_0)^2}{\omega_0^2}\right], \quad (12)$$

where I_0 is the peak light intensity at the center (x_0, y_0). ω_0 is the waist radius of the Gaussian beam, representing the radius where the light intensity drops to I_0/e^2 (e is Euler's number).

The light is propagated along the Z-axis. Thus,

$$\frac{\partial I(z)}{\partial z} = -\mu I(z), \quad (13)$$

where μ is the overall absorption coefficient, incorporating the effects of photoinitiators, cured polymers, uncured monomers, and photoabsorbers as

$$\mu = \mu_I C_I + \mu_P \phi + \mu_{AB} \omega_{AB}. \quad (14)$$

Here, C_I is the concentration of PI, and ω_{AB} is the weight ratio of photoabsorbers. The μ_I, μ_P, μ_{AB} are the absorption coefficients of initiators, cured polymers, and photoabsorbers, respectively. The parameters are listed in Table 2.

Table 2. The parameters used in light intensity calculation.

Name	Value	Definition	Units
I_0	198.7	Peak light intensity value	W/m^2
ω_0	42×10^{-6}	Measured beam waist radius	m
μ_I	45.83	Absorption coefficient of photoinitiators [27]	m^2/mol
μ_P	1.8×10^3	Absorption coefficient of polymers [27]	1/ m

A custom MATLAB script was developed to simulate the photopolymerization process. **Fig. 3(a)** and (b) show the simulated ϕ distribution of a voxel with 10 pixels × 10 pixels at the focal plane with curing times of 0.5 s and 1.5 s. The black contours show the position where ϕ reaches the critical value of DoC ϕ_c. Here, ϕ_c is set to 0.15 [31]. The cured width is defined as the distance between two opposite sides of the contour. Fig. 3(d) and (e) show the simulated isosurface of $\phi = \phi_c$ with exposure time of 0.5 s and 1.5 s, respectively. The cured depth is defined as the maximum z-coordinate of the isosurface.

2.4. Model-guided elimination of material interference

The theoretical model was validated by experiments using four materials: VeroClear, TEAA, FT, and F69. Fig. 3(e) and (f) compare the theoretical and experimental depth and width as functions of the exposure time. The cured width is measured by printing blocks with 10 pixels × 10 pixels, while the cured depth is measured by printing overhanging structures (**Fig. S3**). The reaction coefficients K_a ($a = d, i, p, t$) and diffusion coefficients were obtained by fitting the model to experimental width and depth. The fitting of the reaction–diffusion coefficients to the experimental data was performed manually using the Least Squares Method. For each material, the key parameters, K_a ($a = d, i, p, t$) and diffusion coefficient D, were assigned with an initial value and bounded ranges. The sum of squared differences between the simulated and experimental results was computed for both the exposure time–width and exposure time–height curves. The parameters were iteratively adjusted until this sum reached its minimum value, ensuring optimal agreement between the model and experiment.

The model accurately predicts the sizes of printed voxels. As exposure time increases, both depth and width grow, but different resins exhibit varying trends. For example, FT and F69 show a relatively flat increase in depth but a sharp increase in width with exposure time. In contrast, VeroClear and TEAA exhibit larger depth increases with relatively less increase in width compared to FT and F69. The simulated results for all materials can be found in **Movie S1**.

During the multimaterial voxel printing, we observed a common printing error: material interference, where one material occupies the region designated for another. For example, a two-material pattern with intersecting lines (5 pixels wide, VeroBlack) and squares (20 × 20 pixels, VeroBlue) was printed using the same parameters (0.7 seconds of exposure per layer). The microscopic image of the printed sample shows the substantial overlap of square and line areas (Fig. 3(h)). The dashed box highlights the intended square dimensions, but the printed squares are much larger, occupying the space for the line areas. Thus, the material interfaces remain blurred even after rinsing. This interference leads to substantial differences in both structure and material volume fraction compared to the design. The phenomenon results from

different evolutions of the printing sizes of VeroBlack and VeroBlue under the same printing parameters (Fig. 3(j) and (k)).

Based on the theoretical model, the optimized printing parameters were selected. The ideal exposure time is determined by identifying the intersection of the theoretical curves with the target width (500 μm for 10-pixel wide features) (Fig. 3(c) and (j)). The corresponding cured depth is then calculated using these exposure times (Fig. 3(f) and (k)). Table 3 lists optimized voxel printing parameters. The layer thicknesses of the VeroBlue and VeroBlack are set to 50 μm to ensure strong bonding. A snapshot and microscopic image of the printed sample using the optimized printing parameters are shown in Fig. 3(i), exhibiting clear material interface boundaries. It is worth mentioning that the coupled Gaussian field–reaction–diffusion framework is based on fundamental free-radical photopolymerization kinetics incorporating Beer–Lambert optical attenuation and short-time diffusion effects. Therefore, it is not limited to a specific resin system. In this study, the model is validated using six different photopolymer materials, and the predicted voxel dimensions showed good agreement with experimental measurements. Hence, the proposed model is expected to be universally applicable to other material systems that follow similar photopolymerization mechanisms.

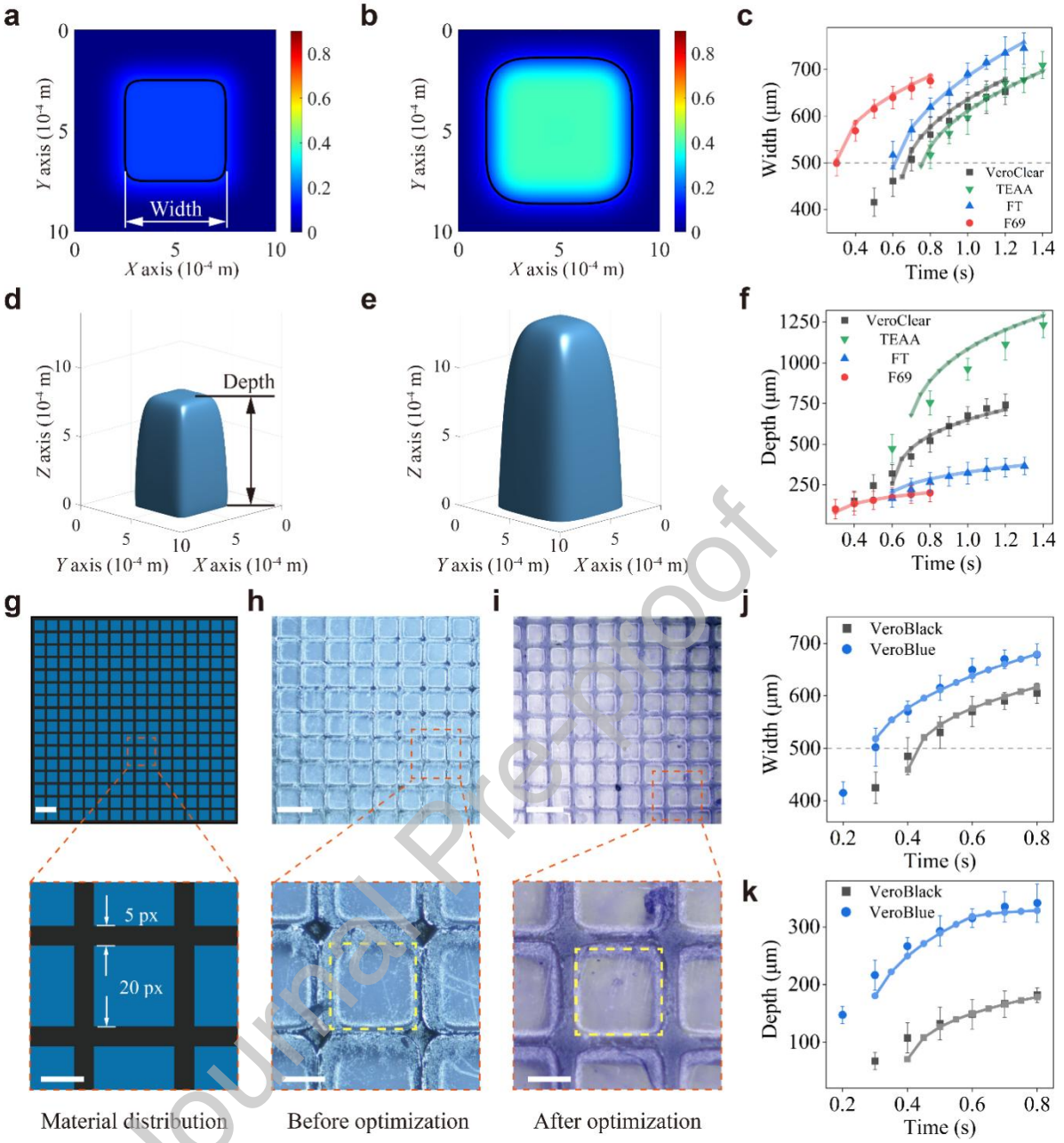

Fig. 3. Theoretical model for optimizing printing parameters. (a), (b) The simulated DoC distribution of TEAA at the focal plane (z = 0) with an exposure time of 0.5 s and 1.5 s, respectively. The black contours show the location of DoC $\phi = \phi_c$. (c) The comparison between the simulated (solid lines) and experimental (markers) width for four materials. (d), (e) The simulated isosurface of $\phi = \phi_c$ with exposure time of 0.5 s and 1.5 s, respectively. (f) The comparison between the simulated and experimental depth for four materials. (g) The designed pattern featuring a minimal size of 5 px. (h), (i) The snapshot and microscopic image of the printed sample before and after parameter optimization, respectively. The dashed boxes show the desired dimension. (Scale bar: upper part 2 mm, lower part 0.5 mm) (j), (k) The comparison between the simulated (solid lines) and experimental (markers) width and depth for VeroBlack and VeroBlue.

Table 3. The optimized printing parameters for various materials.

Materials	VeroClear	FT	F69	TEAA	VeroBlue	VeroBlack
Time (s)	0.68	0.62	0.3	0.77	0.3	0.44
Maximum layer thickness (μm)	411	217	84	814	180	101

2.5. Voxel composite material

The developed rotation-rinsing printing method, coupled with model-based exposure parameters optimization, overcomes interfacial contamination and enables high-fidelity voxel printing with clear boundaries. The mechanical properties of the voxel structures were then analyzed using a developed voxel-based Python-assisted FE simulation framework. FE simulations were conducted in Abaqus 2020 (Dassault Systems, Waltham, MA, USA). Home-written Python scripts partition the structures using desired voxel sizes, allocate the material according to the desired input, and perform calculations and post-processing.

Voxel composite cuboids (32 mm × 6 mm × 1 mm) were designed to validate the FE simulation framework (**Fig. 4(a)**). The voxels were randomly allocated, with each unit measuring 0.5 mm × 0.5 mm and a height of 100 μm. Three materials with different Young's moduli were chosen to print the voxel cuboids: VeroClear (1.1 GPa), FT (1.4 MPa), and TEAA (0.4 MPa) (Fig. 4(d)). Two rigid-soft material combinations: FT-TEAA pair, and VeroClear-FT pair were printed with various ϕ_r (volume ratios of rigid material) ranging from 0% to 100%. The snapshots and microscopic images of the two pairs can be found in **Fig. S4**, showing reliable printing quality. Fig. 4(b) and 4(c) show the uniaxial tensile stress–strain curves for the voxel cuboids made from the FT-TEAA pair, and the VeroClear-FT pair, respectively. Voxel-based simulations were conducted, and the material distributions in the simulations are shown in Fig. S4. The FE-simulated stress–strain curves show good agreement with the experimental curves for the FT-TEAA pair. The discrepancy between the experimental and simulated curves in Fig. 4(c) mainly arises from local fractures that occur during the uniaxial tensile tests, which

were not considered in the FE simulations. Local fractures tend to initiate at regions with large modulus mismatch or imperfect interfacial bonding between adjacent voxels of different materials (**Fig. S6**). Consequently, the experimental stress values are slightly lower than the simulated ones, particularly beyond the elastic regime. The corresponding elastic moduli E, calculated from the stress–strain data, are shown in Fig. 4(e) and (f). The elastic moduli of the composite structures vary continuously between the moduli of the rigid and elastic materials, which span four orders of magnitude.

To quantitatively evaluate the mesh sensitivity of the Python-assisted FE framework, simulations were performed with different mesh refinement levels with n = [1, 2, 4, 5, 6, 8]. Given the voxel size of 0.5 mm, the corresponding mesh sizes were 0.5, 0.25, 0.125, 0.1, 0.083, and 0.0625 mm. The relationship between voxel size and mesh size is illustrated in **Fig. S5(a)**. The simulated stress-strain curves in Fig. S5(b) exhibit only minor variations among different mesh sizes. The stress values at 100% strain are summarized in Fig. S5(c). The stress converges rapidly when n is larger than 4. The computational time rises from approximately 10 minutes for n = 5 to about 2 hours for n = 8. The dashed lines in Fig. S5(c) represent the 0.5% error threshold, indicating that the simulations with $n \geq 5$ achieve sufficient accuracy. Therefore, n = 5 was selected as an optimal balance between computational efficiency and numerical accuracy.

The transition zone of the rigid-soft material was analyzed using three different voxel distributions: a direct connection (referred to as "Simple"), a uniform region with ϕ_r = 50% (referred to as "Uniform"), and a graded region where ϕ_r gradually ranges from 0% to 100% (referred to as "Graded"). The sample slice image and the microscopic images are shown in Fig. 4(g), (i), (k). VeroBlack (black) and TEAA (transparent) were used. It is worth mentioning that the differences in the local color are caused by the different distribution of the black voxel along the z-axis rather than contamination. Snapshots show that the boundaries between individual voxels remain clear, even with small voxel sizes. Fig. 4(m) shows the experimental and FE-simulated tensile stress–strain curves for the voxel composite cuboids. The simulated and experimental deformed shapes demonstrate good agreement (Fig. 4(h), (j), (l)).

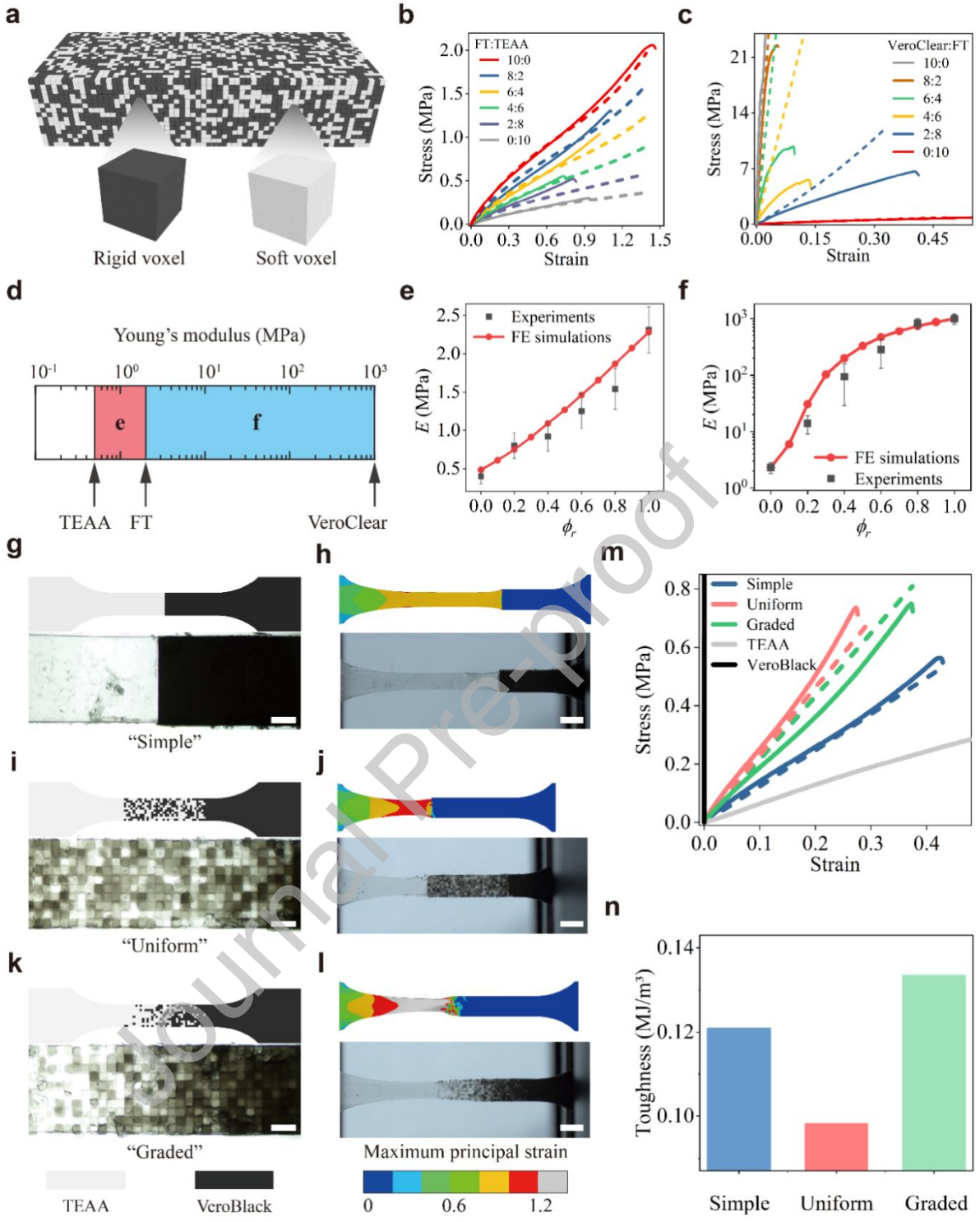

Fig. 4. Python-assisted FE simulation guided design for voxel composites. (a) Schematic illustration of the voxel cuboid comprised of randomly distributed rigid and soft voxels. (b), (c) The experimental (solid lines) and FE-simulated (dashed lines) stress–strain curves of voxel composites VeroClear-FT and FT-TEAA. (d) The Young's moduli of the chosen materials (e), (f) The experimental (markers) and FE-simulated (solid lines) E as functions of ϕ_r for voxel

composites VeroClear-FT and FT-TEAA. (g), (i), (k) Design and microscopic images of two-material dogbone samples with 3 types of transitional regions: simple, uniform, and graded. (Scale bar: 1.5 mm). (h), (j), (l) Experimental and simulated deformation of the dogbone samples before fracture. (Scale bar: 5 mm) (m) Experimental and simulated tensile stress–strain curves of samples with varying transitional designs. (n) Toughness comparison for the three transitional designs.

Note that although the volume fraction is identical for all three structures, their mechanical behaviors differ significantly due to the voxel distributions. Experimental toughness, calculated from the areas under the stress–strain curves, is shown in Fig. 4(n). The "Graded" design exhibited the highest toughness among the three samples, demonstrating that gradual transitions in material properties enhance the overall mechanical performance of the rigid-soft connection. A snapshot of the fractured sample (Fig. S4) shows that the fracture occurs away from the material interface, indicating strong interface bonding.

2.6. An ML-EA design method for multimaterial controllable buckling structures

The validated Python-assisted FE simulation framework was then used to inversely design mechanical properties using voxel distributions. Conventional optimization methods would face tremendous computational costs when dealing with the vast design space of voxels [33,43,44]. Here, an ML-EA design method was developed. A typical buckling structure, consisting of three hinges and two blocks, was taken as an example (**Fig. 5(a)**). Each hinge has a uniform width t = 4 mm and height h = 8 mm, and the overall height and thickness of the structure are L = 75 mm and T = 2 mm, respectively. Upon compression in the vertical direction, the blocks rotate due to the buckling instability of the hinges.

Two materials, VEAA and F69, were used. VEAA exhibits elastoplastic behavior, with an elastic modulus of 200 MPa, a yield stress of 8 MPa, and a tangent modulus of 16 MPa after yielding (**Fig. S7**). F69 demonstrates hyperelastic behavior, described using a two-parameter Mooney-Rivlin model with C_{10} = 0.1215 MPa and C_{01} = 0.9586 MPa. Fig. 5(b) shows the experimental (solid curves) and FE simulated (dashed curves) force–strain (u/L) curves under compression for the structures made from VEAA and F69, respectively. The two different

materials show distinct behaviors: for the hyperelastic F69 structure, the post-buckling stiffness remains positive, leading to a continuing increase in force. In contrast, buckling occurs near the yield point for the elastoplastic VEAA structure, causing a sharp load decrease concomitant with buckling [45]. The simulated and experimental deformations of the F69 structure are compared in Fig. 5(c).

Previous work has explored the buckling behaviors of similar structures. Here, we demonstrate that mechanical behaviors can be controlled by designing voxel distributions. Three parameters were used to characterize the force–strain curves: the force F_1 at buckling, the force F_2 at a compression strain of 10%, and the area A under the force–strain curves (Fig. 5(b)). The ML-EA workflow is illustrated in Fig. 5(e). First, a dataset is generated for the ML model. The buckling structure is partitioned into 26 areas (Fig. 5(d)), each assigned a code 0 or 1 to represent the two materials. By varying voxel combinations, various force–strain curves can be designed. The input consists of randomly generated arrays (1×26 in size, with 4000 samples) representing material voxel combinations. The Python script reads the arrays, allocates materials accordingly, and automatically computes the corresponding force–strain curves via FE simulation. The outputs are constructed by extracting three features (F_1, F_2, and energy absorption) from each curve.

Next, an ANN-based ML model is established to learn the mapping between material distribution and mechanical response and to function as a surrogate model. The ML model comprises two feedforward layers: a hidden layer of 50 neurons and a linear regression layer. The Bayesian regularization is used in training the ML model. The mean squared error (MSE) functions as the loss function and converges to a steady state, as shown in Fig. 5(g). A high coefficient of determination ($R^2 = 0.9993$) is observed in Fig. 5(h), showing that the developed ML model can accurately capture the underlying pattern of the dataset.

Lastly, the EA is employed to optimize the material distribution for achieving the desired mechanical performance. The optimization begins by generating a generation of 150 individuals, where each individual corresponds to a distinct material distribution. The generation evolves through selection, crossover, and mutation after a customized fitness

function evaluates each individual. For energy absorption applications, the desired force–strain curves generally require a small force change between F_1 and F_2, while maximizing the total absorbed energy (A). Thus, the fitness function value (*Fval*) is formulated as:

$$Fval = \left[(F_1 - F_2)/a\right]^b - cA, \tag{15}$$

here, $a = 3$, $b = 5$ and $c = 100$. Fig. 5(i) shows that the *Fval* decreases when the generation index grows. The optimization process stops when the change in *Fval* reaches the function tolerance 10^{-6}. The computational time of a single FE simulation is approximately 2 minutes. Thus, a conventional optimization process requiring 100 iterations would take about 200 minutes in total. In contrast, the training of the machine learning model and the subsequent evolutionary optimization process takes around 2.5 minutes, which is around 80 times faster than conventional FE-based optimization.

The parameters a, b, and c were introduced to normalize the force difference and balance two competing objectives: minimizing force difference (F_1−F_2) and maximizing the area A of the force–strain curve. The constant $a = 3$ specifies that the targeted force difference should be less than 3N. The constants b and c determine the weighting of the two terms. To justify these parameters, a systematic sensitivity analysis was performed by varying b from 2 to 8 and c from 20 to 200. For each parameter pair (b, c), the evolutionary algorithm was performed using the trained neural network. The resulting optimized data (70 data points, marked as red stars) were compared with the full database of simulated data (3000 data points, marked as blue circles) in the (F_1−F_2, A) space (**Fig. S8**). The optimized data achieve a large area A while restricting the force differences, which is challenging to achieve by manually guessing the material distribution. On the other hand, the optimized results exhibit only minor variations across the tested range, confirming the robustness of the fitness function.

Although the optimized data are concentrated within a narrow region, several distinct material distributions emerged. The 70 parameter pairs generate 4 unique material distributions (**Table S1**), which were further analyzed via FE simulation. The resulting force-strain curves (**Fig. S9**) show similar profiles, and all achieve the desired performance. The FE simulated

force–strain curves are shown in Fig. 5(j) for the material array in the 1st, 10th, 50th, and 100th generations. The multimaterial buckling structure is printed using the optimal material distribution. The experimental curve agrees well with the FE simulated curve before 5% strain. The snapshots of the simulated and experimental deformations are shown in Fig. 5(k) and agree well. The decrease in the experimental force after 5% strain may be caused by the detachment of the top left beam (Fig. 5(k)).

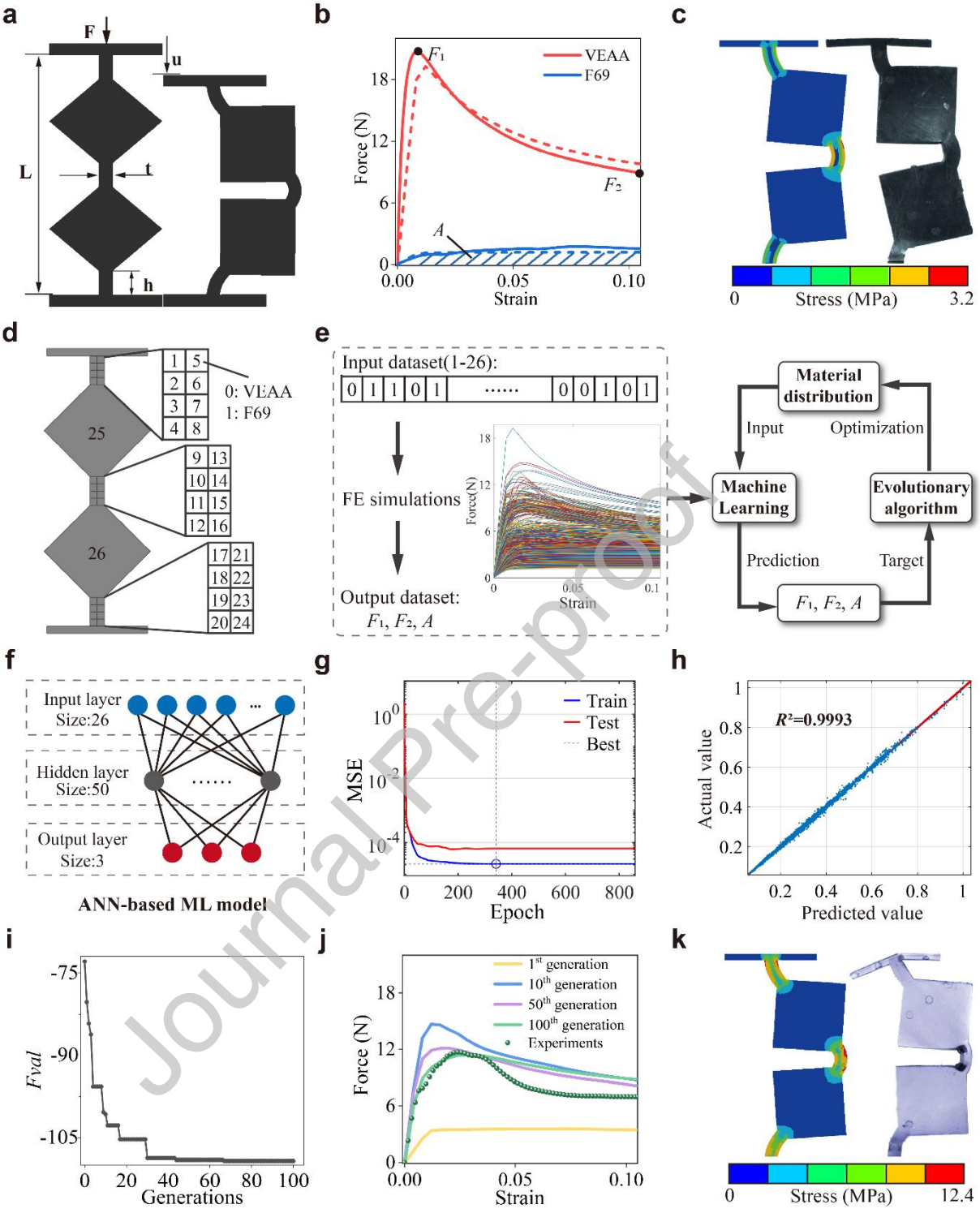

Fig. 5. Design method of the multimaterial controllable buckling structure using a machine learning model and evolutionary algorithm (ML-EA). (a) The schematic illustration of the buckling structure with three hinges and two blocks. (b) The simulated and experimental force–strain curves of the uniaxial compression test using single material VEAA and F69. (c) The comparison between the experimental and simulated buckling deformation of the F69 case. (d) Schematic illustration of the material distribution and the index of the material distribution array.

(e) The training process and the workflow of the optimization process. (f) The architecture of the ANN-based ML model. (g) The MSE function of the ML model during the training process. (h) The linear regression analysis of the ML model. The coefficient of determination (R^2 = 0.9993) shows good prediction capability. (i) The evolution of *Fval* during the EA-based optimization process. (j) The FE simulated results using the optimized results in the 1st, 10th, 50th, and 100th generations and the experimental result. (k) The snapshots of the simulated and experimental deformations using the optimized material distribution.

3. Materials and methods

UV curable resin: The commercial photo-curable polymer resins include VeroBlue (rigid blue polymer, Stratasys, USA), VeroBlack (rigid black polymer, Stratasys, USA), VeroClear (rigid transparent polymer, Stratasys, USA), F69 (soft black polymer, Flashshore, China), TangoPlus (soft translucent polymer, Stratasys, USA). The mixed commercial photo-curable polymer resins include FT, VEAA, and TEAA. The FT is a mixture of F69 and TangoPlus with a mass ratio of 1:1. The mixture VEAA consists of 80 wt% VeroClear and 20 wt% EAA (epoxy aliphatic acrylate, Ebecryl 113, Allnex, USA). 0.02 wt% Sudan I is added to the VEAA mixture. The mixture TEAA consists of 60 wt% Tango and 40 wt% EAA. The mixtures mentioned above are magnetically stirred at 40 °C for at least 6 hours after mixing all the ingredients. The viscous EAUD hybrid resin consists of 60 wt% EAA and 40 wt% AUD (Ebecryl 8413, Allnex, USA). 2 wt% of Irgacure 819 (Sigma-Aldrich, USA) is added to the mixture as the photoinitiator.

Multimaterial DLP printing system: The linear translation stage LTS300 (ThorLabs, USA) moves the printing platform. The servo motor EC-i 52 (Maxon, Germany) is responsible for spinning the platform to remove the residual resin and rinsing agent. A DLP projector PRO6500 (Wintech, China) is used to project the corresponding slice image to the bottom of the resin tank. The PFA membranes are purchased from local retailers.

Resin thickness measurement: Experiments were conducted using a KW-4C spin coater (SETCAS, China) with facing-up circular acrylic substrates (36 mm diameter) to enable

accurate dosage. The base thickness of the substrates ("t_1") was measured with a micrometer screw gauge (accuracy: 1 μm). For each test, 1 mL of resin was dispensed onto the substrate. 5 mL of 95% ethanol was dispensed onto the plate for the rinsing case. The rotational speed varied from 3000 to 10000 rpm, and the acceleration was 3000 rpm/s for all speeds. Two protocols were used: 1) 16s of spinning for the non-rinsed protocol. 2) 8s of spinning, dispensing ethanol, another 8s of spinning (total 16s). No immersion bath was employed in our experiments, so the immersion depth is not applicable. After spinning, the residual film was fixed using a 405 nm UV exposure for 3 minutes. The thicknesses of substrate and the residual resin were measured ("t_2"), and the residual resin thickness was calculated ("$t_2 - t_1$").

FE simulations: For the FE simulation in Fig. 4, 3D stress conditions and hybrid tetrahedral elements (C3D4H) are used. The mesh size equaled the voxel size divided by 5 (0.1 mm). For FE simulation in Fig. 5, plane stress conditions and modified quadratic triangular elements (CPS6M) are used. The mesh size equaled the voxel size divided by 5 (0.4 mm). The static step is used, and a displacement imperfection is introduced (0.1 mm).

Uniaxial tensile and compression tests: In the tensile tests of Fig. 4, voxel composites were printed with hard material at the ends for clamping. The uniaxial tensile tests were conducted on a universal material testing machine (Instron 68SC-2, USA) at room temperature with a speed of 10 mm/min. For the compression tests in Fig. 5, an acrylic slot lubricated with silicone oil was used to restrict bending directions. The bottom bar of the structures was clamped, while the top bar was free and was compressed by another acrylic plate.

Relative brightness calculation: RB was calculated using the ITU BT.709 standard: RB = 0.299R + 0.587G + 0.114B, where R, G, and B are RGB values read from the images. The average RB values of the black area for the two samples are both around 0.07, indicating that the two images have the same exposure value without modification.

4. Conclusion

In this work, a multimaterial DLP 3D printing platform is developed that integrates centrifugal force-assisted resin removal and liquid-based rinsing to eliminate cross-contamination between different materials. This approach enables the fabrication of multimaterial voxel structures even for high-viscosity materials. A multiphysics model considering chemical reactions, diffusion effects, and Gaussian light fields is proposed to accurately predict voxel sizes. Using the theoretical model, optimal printing parameters for each resin are predicted to avoid under-curing-induced structural failure and over-curing-induced material interference. By combining the fabrication technology and theoretical model, voxel structures can be accurately fabricated, which can facilitate the design of various behaviors. A Python-assisted FE simulation combined with an ML-EA method is presented to inversely design the voxel distribution across a vast design space. A buckling structure is taken as an example to design optimal stress–strain curves for energy absorption. This work paves the way for the fabrication, modeling, and design of 3D-printed voxel structures.

References

[1] R.L. Truby, J.A. Lewis, Printing soft matter in three dimensions, Nature 540(7633) (2016) 371-378.
[2] T.H. Ware, M.E. McConney, J.J. Wie, et al., Voxelated liquid crystal elastomers, Science 347(6225) (2015) 982-984.
[3] N.M. Larson, J. Mueller, A. Chortos, et al., Rotational multimaterial printing of filaments with subvoxel control, Nature 613(7945) (2023) 682-688.
[4] M.A. Skylar-Scott, J. Mueller, C.W. Visser, et al., Voxelated soft matter via multimaterial multinozzle 3D printing, Nature 575(7782) (2019) 330-335.
[5] H. Ye, Q. Liu, J. Cheng, et al., Multimaterial 3D printed self-locking thick-panel origami metamaterials, Nat. Commun. 14(1) (2023) 1607.
[6] J. Mueller, J.A. Lewis, K. Bertoldi, Architected multimaterial lattices with thermally programmable mechanical response, Adv. Funct. Mater. 32(1) (2022) 2105128.
[7] J. Schwartz, A. Boydston, Multimaterial actinic spatial control 3D and 4D printing, Nat. Commun. 10(1) (2019) 791.
[8] J. Chen, L. Zhao, K. Zhou, Multi-jet fusion 3D voxel printing of conductive elastomers, Adv. Mater. 34(47) (2022) 2205909.
[9] C.E. Gregg, D. Catanoso, O.I.B. Formoso, et al., Ultralight, strong, and self-reprogrammable mechanical metamaterials, Sci. Rob. 9(86) (2024) eadi2746.
[10] R. Khodambashi, Y. Alsaid, R. Rico, et al., Heterogeneous hydrogel structures with spatiotemporal reconfigurability using addressable and tunable voxels, Adv. Mater. 33(10) (2021) 2005906.
[11] Y.L. Kong, Multi-material 3D printing guided by machine vision, Nature Publishing Group UK London, 2023.
[12] J. Zhu, Y. He, Y. Wang, et al., Voxelated bioprinting of modular double-network bio-ink droplets, Nat. Commun. 15(1) (2024) 5902.
[13] L. Dong, J. Wang, D. Wang, Modeling and design of three-dimensional voxel printed lattice metamaterials, Addit. Manuf. 69 (2023) 103532.
[14] L.T. Smith, R.B. MacCurdy, Digital Multiphase Composites via Additive Manufacturing, Adv. Mater. (2024) 2308491.
[15] C. Zhu, H.B. Gemeda, E.B. Duoss, et al., Toward Multiscale, Multimaterial 3D Printing, Adv. Mater. (2024) 2314204.
[16] K. Zub, S. Hoeppener, U.S. Schubert, Inkjet printing and 3D printing strategies for biosensing, analytical, and diagnostic applications, Adv. Mater. 34(31) (2022) 2105015.
[17] C. Bader, D. Kolb, J.C. Weaver, et al., Making data matter: Voxel printing for the digital fabrication of data across scales and domains, Sci. Adv. 4(5) (2018) eaas8652.
[18] Q. Ge, Z. Chen, J. Cheng, et al., 3D printing of highly stretchable hydrogel with diverse UV curable polymers, Sci. Adv. 7(2) (2021) eaba4261.
[19] K. Kowsari, S. Akbari, D. Wang, et al., High-efficiency high-resolution multimaterial fabrication for digital light processing-based three-dimensional printing, 3D Print. Addit. Manuf. 5(3) (2018) 185-193.

[20] G. Lipkowitz, T. Samuelsen, K. Hsiao, et al., Injection continuous liquid interface production of 3D objects, Sci. Adv. 8(39) (2022) eabq3917.
[21] D. Han, C. Yang, N.X. Fang, et al., Rapid multi-material 3D printing with projection micro-stereolithography using dynamic fluidic control, Addit. Manuf. 27 (2019) 606-615.
[22] C. Carbonell, M. Linares-Moreau, S.M. Borisov, et al., Multimaterial Digital-Light Processing of Metal-Organic Framework (MOF) Composites: A Versatile Tool for the Rapid Microfabrication of MOF-Based Devices, Adv. Mater. 36(45) (2024) 2408770.
[23] J. Cheng, R. Wang, Z. Sun, et al., Centrifugal multimaterial 3D printing of multifunctional heterogeneous objects, Nat. Commun. 13(1) (2022) 7931.
[24] S.M. Montgomery, F. Demoly, K. Zhou, et al., Pixel-Level Grayscale Manipulation to Improve Accuracy in Digital Light Processing 3D Printing, Adv. Funct. Mater. 33(17) (2023) 2213252.
[25] Y. Xu, F. Qi, H. Mao, et al., In-situ transfer vat photopolymerization for transparent microfluidic device fabrication, Nat. Commun. 13(1) (2022) 918.
[26] J. Wu, Z. Zhao, C.M. Hamel, et al., Evolution of material properties during free radical photopolymerization, Journal of the Mechanics and Physics of Solids 112 (2018) 25-49.
[27] S.M. Montgomery, C.M. Hamel, J. Skovran, et al., A reaction–diffusion model for grayscale digital light processing 3D printing, Extreme Mech. Lett. 53 (2022) 101714.
[28] M.M. Emami, D.W. Rosen, Modeling of light field effect in deep vat polymerization for grayscale lithography application, Addit. Manuf. 36 (2020) 101595.
[29] R. Melentiev, G. Harakály, J. Stögerer, et al., High-resolution metal 3D printing via digital light processing, Addit. Manuf. 85 (2024) 104156.
[30] H. Zhu, Y. Guo, Z. Chen, et al., A photo-chemo-mechanical coupling constitutive model for photopolymerization-based 3D printing hydrogels, Journal of the Mechanics and Physics of Solids 192 (2024) 105830.
[31] X. Fan, M. Zhang, L. Hu, et al., Modeling and spatio-temporal optimization of grayscale digital light processing 3D-printed structures with photobleaching resins, Addit. Manuf. 99 (2025) 104659.
[32] H. Kansara, M. Liu, Y. He, et al., Inverse design and additive manufacturing of shape-morphing structures based on functionally graded composites, Journal of the Mechanics and Physics of Solids 180 (2023) 105382.
[33] D. Wang, L. Dong, G. Gu, 3D printed fractal metamaterials with tunable mechanical properties and shape reconfiguration, Adv. Funct. Mater. 33(1) (2023) 2208849.
[34] D. Kokkinis, M. Schaffner, A.R. Studart, Multimaterial magnetically assisted 3D printing of composite materials, Nat. Commun. 6(1) (2015) 8643.
[35] Y.F. Zhang, N. Zhang, H. Hingorani, et al., Fast-response, stiffness-tunable soft actuator by hybrid multimaterial 3D printing, Adv. Funct. Mater. 29(15) (2019) 1806698.
[36] J.W. Boley, W.M. Van Rees, C. Lissandrello, et al., Shape-shifting structured lattices via multimaterial 4D printing, PNAS 116(42) (2019) 20856-20862.
[37] X. Sun, L. Yue, L. Yu, et al., Machine Learning-Evolutionary Algorithm Enabled Design for 4D-Printed Active Composite Structures, Adv. Funct. Mater. 32(10) (2022) 2109805.

[38] M. Wang, W. Li, L.S. Mille, et al., Digital Light Processing Based Bioprinting with Composable Gradients, Adv. Mater. 34(1) (2022) 2107038.
[39] C.-f. He, T.-h. Qiao, X.-c. Ren, et al., Printability in Multi-material Projection-Based 3-Dimensional Bioprinting, Research 8 (2025) 0613.
[40] M. Yang, L. Chu, Y. Zhuang, et al., Multi-Material Digital Light Processing (DLP) Bioprinting of Heterogeneous Hydrogel Constructs with Perfusable Networks, Adv. Funct. Mater. 34(32) (2024) 2316456.
[41] M. Buback, A.M. van Herk, Radical polymerization: kinetics and mechanism, John Wiley & Sons2007.
[42] C.N. Bowman, C.J. Kloxin, Toward an enhanced understanding and implementation of photopolymerization reactions, AlChE J. 54(11) (2008) 2775-2795.
[43] D. Athinarayanarao, R. Prod'hon, D. Chamoret, et al., Computational design for 4D printing of topology optimized multi-material active composites, npj Comput. Mater. 9(1) (2023) 1.
[44] L. Dong, D. Wang, Optimal design of three-dimensional voxel printed multimaterial lattice metamaterials via machine learning and evolutionary algorithm, Phys. Rev. Appl. 18(5) (2022) 054050.
[45] W. Liu, S. Janbaz, D. Dykstra, et al., Harnessing plasticity in sequential metamaterials for ideal shock absorption, Nature (2024) 1-6.

Acknowledgment

This work was supported by the National Natural Science Foundation of China (Grant No. T2522018, 52025057 and 52275025), the Science and Technology Commission of Shanghai Municipality (Grant No. 25XF3200400), the National Key Research and Development Program of China (No. 2022YFB4700900), the State Key Laboratory of Mechanical System and Vibration (Grant No. MSVZD202401), Interdisciplinary of Medicine and Engineering Foundation of Shanghai Jiao Tong University (YG2024QNA21), and Xplorer Prize.

Graphical Abstract

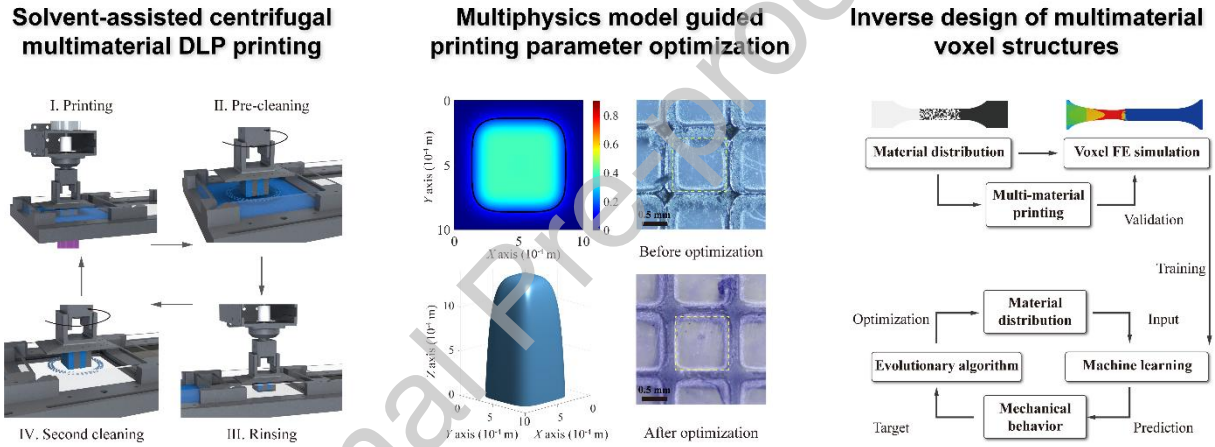

Personal Profile

☐ Mengjie Zhang

Mengjie Zhang received the B.Eng degree from the College of Mechanical Engineering of Chongqing University, China, in 2020. He is currently working toward the Ph.D. degree in the School of Mechanical Engineering, Shanghai Jiao Tong University, China. His current research interests include multi-material 3D printing and soft robots.

☐ Dong Wang (BRID: 06835.00.16987)

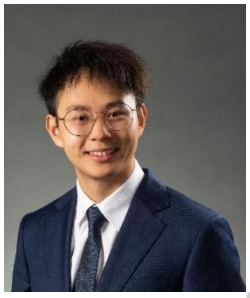

Dong Wang received the B.Eng degree in mechanical engineering from Zhejiang University China, in 2010,and the Ph.D. degree in mechanical engineering from Nanyang Technology University, Singapore, in 2015.

He is currently working as an Associate Professor with the School of Mechanical Engineering, Shanghai Jiao Tong University, China. His research interests include 4D printing and soft robotics.

☐ Qi Ge (BRID: 07329.00.75879)

Dr. Ge received the B.E. degree in Engineering Mechanics from Tongji University, Shanghai, China, in 2006, the M.S. degree in Solid Mechanics from Zhejiang University, Hangzhou, China, in 2008, and the Ph.D. degree in Mechanical Engineering from University of Colorado at Boulder (CU Boulder), U.S.A. He was postdoctoral research at CU Boulder, Massachusetts

Institute of Technology, and Singapore University of Technology and Design (SUTD), respectively. Then, he joined to SUTD as an assistant professor. Since 2019, Dr. Ge moved to Southern University of Science and Technology where he currently is working as a professor, and the associate head for research at Department of Mechanical and Energy Engineering. Dr. Ge also severs as the director of Shenzhen Key Laboratory for Additive Manufacturing of High-Performance Materials, as well as editors of International Journal of Extreme Manufacturing, Microsystems & Nanoengineering. Dr. Ge's research interests include 4D printing and its applications to soft robotics and flexible electronics, and he is recognized as Elsevier Most Cited Chinese Researcher.

☐ Guoying Gu (BRID: 03253.00.69369)

Dr. Gu received the B.E. degree in electronic science and technology from Shanghai Jiao Tong University, Shanghai, China, in 2006 and Ph.D. degree in mechatronic engineering from Shanghai Jiao Tong University, Shanghai, China, in 2012, respectively. Since October 2012, he has been with Shanghai Jiao Tong University, where he is currently a Professor. He was a Humboldt Postdoc Fellow with the University of Oldenburg, Oldenburg, Germany. He was a Visiting Scholar with the Massachusetts Institute of Technology, the National University of Singapore, and the Concordia University. His research interests include soft robotics, bioinspired robot design and motion control, smart materials actuators and sensors, and additive manufacturing with soft materials. Dr. Gu is the recipient of multiple awards, including Young Changjiang Scholar of the Chinese Ministry of Education, National Science Fund for Excellent Young Scholars, and the first prize of Natural Science of Ministry of Education. He is currently an Associate Editor for International Journal of Advanced Robotic Systems.

Declaration of Interest Statement

☒ The authors declare that they have no known competing financial interests or personal relationships that could have appeared to influence the work reported in this paper.

☐ The author is an Editorial Board Member/Editor-in-Chief/Associate Editor/Guest Editor for this journal and was not involved in the editorial review or the decision to publish this article.